MEDICAL ROBOTS

Multifunctional biohybrid magnetite microrobots for imaging-guided therapy

Xiaohui Yan,[1] Qi Zhou,[2] Melissa Vincent,[3] Yan Deng,[4] Jiangfan Yu,[1] Jianbin Xu,[5] Tiantian Xu,[1] Tao Tang,[4] Liming Bian,[1,5] Yi-Xiang J. Wang,[6] Kostas Kostarelos,[3] Li Zhang[1]*

Magnetic microrobots and nanorobots can be remotely controlled to propel in complex biological fluids with high precision by using magnetic fields. Their potential for controlled navigation in hard-to-reach cavities of the human body makes them promising miniaturized robotic tools to diagnose and treat diseases in a minimally invasive manner. However, critical issues, such as motion tracking, biocompatibility, biodegradation, and diagnostic/therapeutic effects, need to be resolved to allow preclinical in vivo development and clinical trials. We report biohybrid magnetic robots endowed with multifunctional capabilities by integrating desired structural and functional attributes from a biological matrix and an engineered coating. Helical microswimmers were fabricated from *Spirulina* microalgae via a facile dip-coating process in magnetite (Fe_3O_4) suspensions, superparamagnetic, and equipped with robust navigation capability in various biofluids. The innate properties of the microalgae allowed in vivo fluorescence imaging and remote diagnostic sensing without the need for any surface modification. Furthermore, in vivo magnetic resonance imaging tracked a swarm of microswimmers inside rodent stomachs, a deep organ where fluorescence-based imaging ceased to work because of its penetration limitation. Meanwhile, the microswimmers were able to degrade and exhibited selective cytotoxicity to cancer cell lines, subject to the thickness of the Fe_3O_4 coating, which could be tailored via the dip-coating process. The biohybrid microrobots reported herein represent a microrobotic platform that could be further developed for in vivo imaging–guided therapy and a proof of concept for the engineering of multifunctional microrobotic and nanorobotic devices.

INTRODUCTION

Scaling down of microrobots and nanorobots able to be navigated into hard-to-reach tissues and other human body cavities currently inaccessible to available devices can offer miniaturized medical tools for biomedical applications such as disease monitoring, targeted drug delivery, minimally invasive surgery, and so on (*1*–*6*). However, miniaturization also brings fundamental engineering challenges such as power sourcing, precise actuation, integration of multifunctionality, and capability of post-injection recovery or biodegradation. To date, several strategies have been reported to address actuation and motion control, including application of external fields (e.g., magnetic, ultrasound, and light) (*7*–*9*), use of biological motors (*10*, *11*), addition of chemical fuel (*2*, *12*), or combinations of the above (*13*, *14*). Among them, magnetic actuation has attracted particular attention because magnetic fields can continuously transmit power to the robotic devices in a wireless manner with high penetrating capacity through the human body harmlessly even at relatively high field strengths (*1*, *3*–*6*, *15*), which has been well justified by the widespread use of magnetic resonance (MR) imaging.

To enable magnetic actuation at the microscale and/or nanoscale, magnetic robots of various structures—such as rigid-flexible nanowires (*13*, *16*, *17*), microspheres (*18*, *19*), ellipsoids (*20*, *21*), helices (*7*, *22*–*25*), filaments (*26*), and even arbitrary shapes (*27*, *28*)—have been developed. Powered by an externally applied magnetic field of certain form (e.g., gradient, oscillating, rotating, or periodically varying), they can be remotely controlled to navigate a variety of complex geometries filled with biological media such as water, blood, serum, and mucus (*1*, *3*–*5*, *7*, *14*, *16*, *20*–*31*). Furthermore, they have the ability to manipulate cellular or subcellular components in either a contact or noncontact fashion (*7*, *16*, *19*, *21*, *26*, *29*). To be applied as versatile tools for in vivo applications, microrobots and nanorobots need to be equipped with further functionalities, such as traceability, biodegradability, and bioactivity. These can be realized with multiple engineering strategies, such as surface decoration, selection of chemical composition, structural design, or a combination of the above (*7*, *18*, *22*–*24*, *29*–*32*). Among all functionalities, of particular interest are absence of cytotoxic response, biodegradability, chemical stability, noninvasive in vivo tracking, targeted drug release, and stimulus-responsive release (*1*–*5*, *7*, *18*, *22*, *24*, *29*–*32*).

Nature offers a rich database of answers to scientific challenges and can inspire solutions. Through natural selection, organisms in real life have evolved sophisticated biological materials featuring not only diverse structures but also a wealth of functionalities, among others, including hydrophobicity/hydrophilicity, reversible adhesion, biodegradability, renewability, magnetotaxis, bioimpedance, fracture resistance, light weight, anti-reflection, and autofluorescence (*33*–*41*). Such nature-abundant functionalities provide interesting options for the engineering of navigable robotic devices (*6*, *10*, *11*, *42*, *43*). We hypothesized that magnetization of biological entities with certain specifications could allow fabrication of magnetic microrobots that incorporate the morphological and functional features from a biological matrix. The fabricated biohybrid agents could be considered essentially composite materials, benefiting from both the biological organic matter and the integrated magnetic component. Furthermore, the inherited functionalities could be tailored for designated applications by controlling the thickness of the magnetic coating during the magnetization process.

[1]Department of Mechanical and Automation Engineering, Chinese University of Hong Kong, Shatin, New Territories, Hong Kong SAR, China. [2]School of Engineering, University of Edinburgh, Edinburgh EH9 3FB, UK. [3]Nanomedicine Laboratory, Faculty of Biology, Medicine and Health, University of Manchester, AV Hill Building, Manchester M13 9PT, UK. [4]Department of Obstetrics and Gynaecology, Chinese University of Hong Kong, Shatin, New Territories, Hong Kong SAR, China. [5]Department of Biomedical Engineering, Chinese University of Hong Kong, Shatin, New Territories, Hong Kong SAR, China. [6]Department of Imaging and Interventional Radiology, Chinese University of Hong Kong, Prince of Wales Hospital, Shatin, New Territories, Hong Kong SAR, China.
*Corresponding author. Email: lizhang@mae.cuhk.edu.hk

Hereafter, we refer to this type of robotic agents as biohybrid magnetic robots (BMRs).

We report BMRs successfully fabricated from microalgae organisms, exhibiting intrinsic fluorescence (see section S1 and figs. S1 to S3), MR signals, natural degradability, and desirable cytotoxicity. These are all critical features in the design of imaging-guided microrobots for therapeutic inventions (*1*–*5*). First, to accomplish navigation in complex biological environments via feedback control, the motion of the microrobots and nanorobots needs to be tracked in vivo and monitored in real time, for which noninvasive multimodal imaging is an effective means. Second, such tiny robots should eventually either degrade themselves to be excreted or be removed without causing undesired side effects. Third, during navigation inside the body, they should not cause hazard to normal cells and, preferably, can inhibit the function of abnormal cells (e.g., malignant).

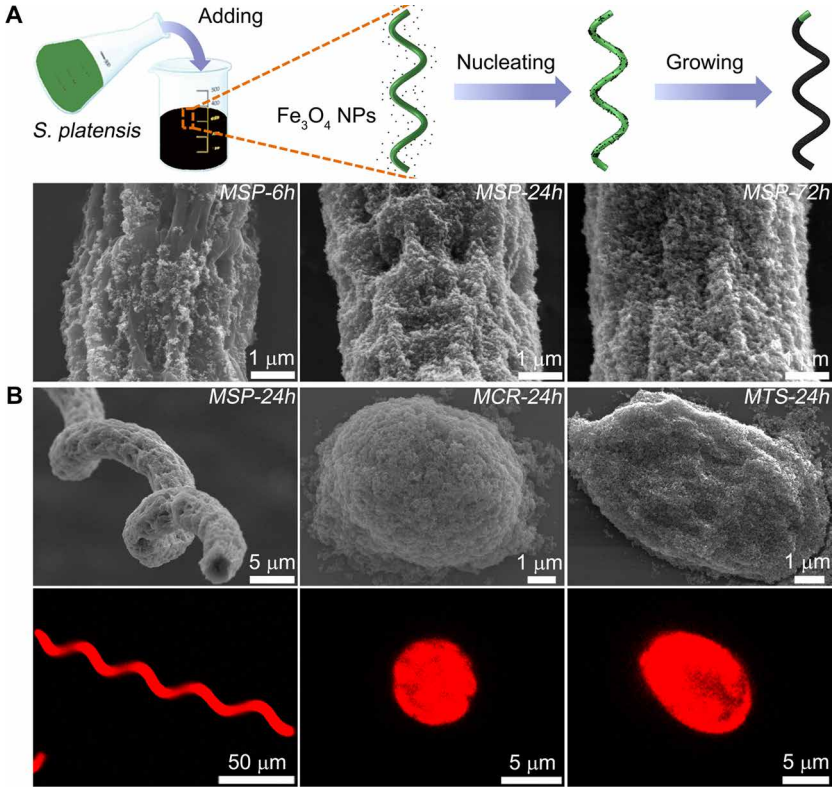

Fig. 1. Dip-coating of *S. platensis*, *C. reinhardtii*, and *T. subcordiformis*. (**A**) Schematic of the dip-coating process of *S. platensis* in a suspension of Fe_3O_4 NPs. Bottom: *MSP-6h/24h/72h* represent the magnetized *S. platensis* subject to 6-/24-/72-hour dip-coating treatments, respectively. As the dipping time increased, the amount of Fe_3O_4 NPs, and hence thickness of the Fe_3O_4 coating on the *S. platensis*, also increased. (**B**) FESEM (top) and fluorescence images (bottom) of *MSP-24h*, *MCR-24h*, and *MTS-24h* samples. The fluorescence images were taken by a Leica SP8 confocal laser scanning microscope with excitation at 552 nm.

RESULTS

Fabrication

Microalgae, organisms with several million distinct species on Earth, have been widely studied and commercialized for their abundance of valuable chemical compositions, for example, pharmaceutically active compounds, high-quality proteins, and natural pigments (*40*, *44*). To fabricate BMRs, an essential step is to magnetize microalgae while preserving their structural features and intrinsic functionalities. For that purpose, we used a facile dip-coating method that bonds Fe_3O_4 nanoparticles (NPs) onto biological surfaces (*41*, *45*). We chose Fe_3O_4 NPs as the magnetic component for their MR contrast, agglomeration-free colloidal suspension, facile surface functionalization, and low cytotoxicity, which means negligible physiological effect on cell or tissue viability (*5*, *31*, *46*).

Previously, we have used *Spirulina platensis* (a microalgae subspecies that features helical shapes) as a biotemplate to fabricate magnetic microswimmers via three steps: deposition of magnetite precursors, annealing, and reduction (*31*). That work only harnessed the structural features of *S. platensis* to build a porous hollow microhelix suitable for cargo loading (the *S. platensis* in the core was removed during the annealing process). Here, we aimed to develop magnetic microrobots with integrated functionalities envisioned for imaging-guided therapy. Simply by coating the biological matrix *S. platensis* with Fe_3O_4 NPs in a controlled fashion, large quantities of such microrobots can be fabricated via a single cost-effective step, without the need of any functionalization processing (although further expansion of the microrobots' functionalities are also possible owing to the easy functionalization nature of Fe_3O_4 NPs).

Figure 1A demonstrates the dip-coating process of *S. platensis* in Fe_3O_4 NP suspensions. The deposited Fe_3O_4 NPs firmly bonded to the surface of *S. platensis* and gradually formed a magnetite coating. For the mechanism and characterization of this process, refer to the Supplementary Materials (section S2, figs. S4 to S8, and table S1). As the field-emission scanning electron microscopy (FESEM) images in Fig. 1A show, the deposition of Fe_3O_4 NPs and therefore the coating thickness on *S. platensis* could be controlled by adjusting the dipping time. Consequently, the magnetic property of the microalgae BMR was also tailored (fig. S7), as were properties of the inherited functionalities such as autofluorescence, MR contrast, biodegradation, and bioactivity. Owing to the easy functionalization feature of Fe_3O_4, further extension of the BMR's functions or designated loading of drugs is also possible by chemically decorating the Fe_3O_4 NPs through functional ligands (*5*, *31*, *32*, *46*).

The dip-coating method also proved feasible for magnetizing other microalgae species, for example, the ellipsoidal *Tetraselmis subcordiformis* and the spherical *Chlamydomonas reinhardtii*. Figure 1B exhibits FESEM and fluorescence images of magnetized *S. platensis MSP-24h* (i.e., dipping in Fe_3O_4 NP suspension for 24 hours), magnetized *C. reinhardtii MCR-24h*, and magnetized *T. subcordiformis MTS-24h*. Apparently, for all of them, the morphological features of the original biological matrices were well preserved after the magnetization. Under confocal laser scanning microscopy (CLSM), homogeneous and intense signals could directly be observed without additional fluorescent markers (the bottom row of Fig. 1B), indicating the uniform deposition of Fe_3O_4 NPs during the dip-coating process and successful inheritance of intrinsic functionalities from the biological matrices. In the following sections, we highlight *MSP* and present its important functionalities for imaging-guided therapy.

Magnetic actuation

The fabricated BMRs had the capacity to be wirelessly actuated and steered using a proper magnetic field according to their shapes and magnetic properties. In view of the literature (*7*, *19*–*21*), we applied a homogeneous rotating magnetic field for the propulsion of *MSP* and *MCR* and a periodically varying one for *MTS*. Both magnetic fields were provided by a custom-made tri-axial Helmholtz coil system. Schematics of the magnetic actuation of the three BMRs are shown in Fig. 2A, followed by superimposed experimental snapshots that delineate the motion trajectories (Fig. 2B). For videos of their locomotion in deionized (DI) water, please refer to movie S1 for *MSP*, movies S2 and S3 for *MCR*, and movie S4 for *MTS*.

We decided to focus on *MSP*, a chiral magnetic microswimmer featuring helical propulsion. Given the state of the art in magnetic field provision, the rotation-coupling propulsion presented by *MSP* is arguably the most promising means of magnetic actuation for future in vivo applications (*47*–*50*). In recent years, extensive research has been carried out on magnetic helical swimmers to explore their potential as microrobotic tools for targeted drug delivery and minimally invasive microsurgery. The *S. platensis* chosen to fabricate *MSP*s is one subspecies of the cyanobacterium *Spirulina*, a microalgae genus that has been widely commercialized as nutritional supplements or food materials. They naturally present helical microstructures with characteristics such as chirality, helical angle, helix diameter, and body length. These features are all sensitive to the living environments of *S. platensis* and can therefore be tuned under laboratory cultivation conditions (*31*), which allows us to select specimens with optimal structural parameters as the biological matrix to fabricate *MSP*s with superior propulsion performance. In addition, the body length of cultivated *S. platensis* can be further adjusted as needed via mechanical dicing or ultrasound treatment (also known as sonication). The former has been used by Gao *et al.* (*51*) to obtain helices with a precise number of pitches from the spiral vessels of vascular plants. In the present study, we explored the latter as a simple

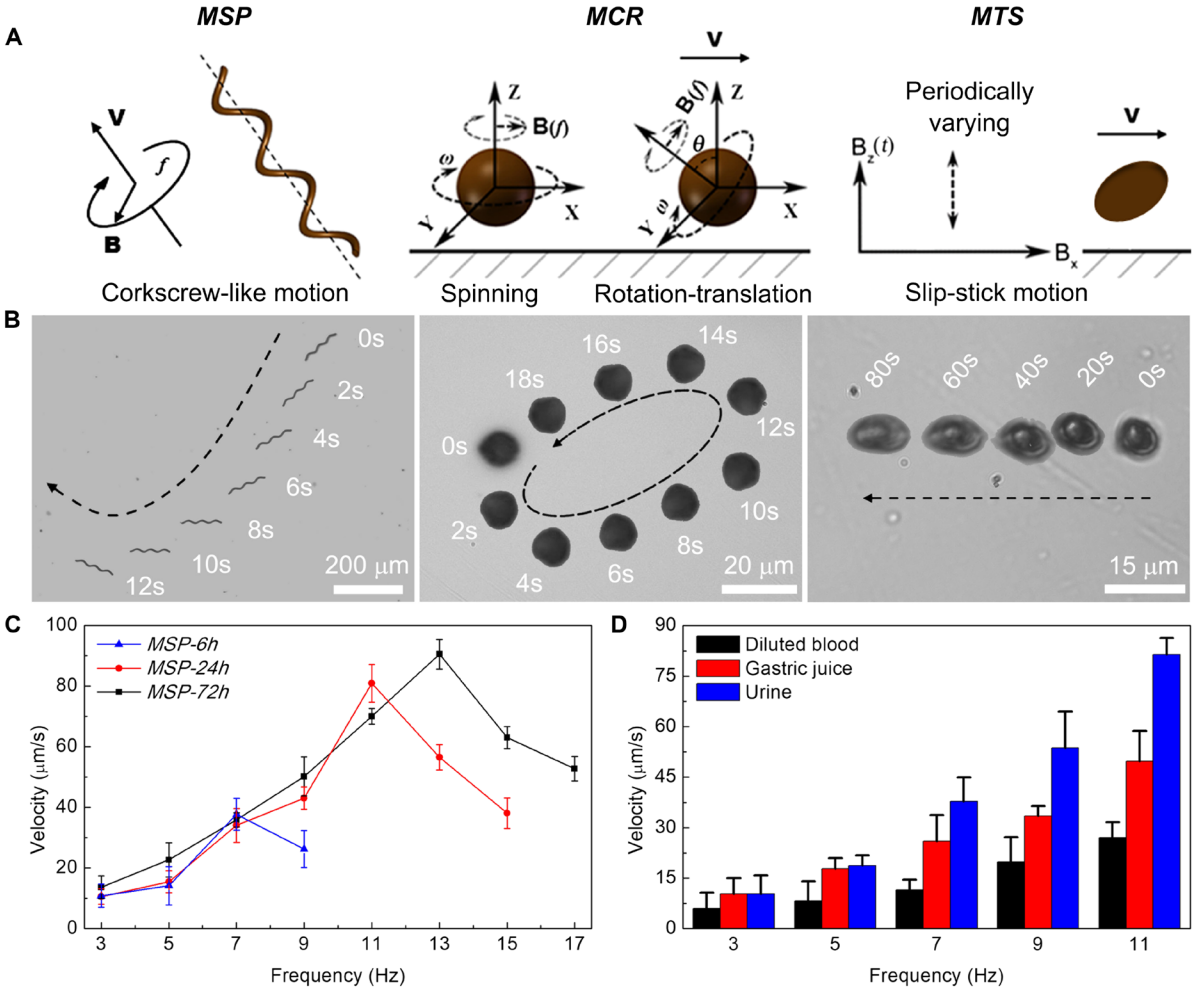

Fig. 2. Magnetic actuation of BMRs. (**A**) Schematics of the magnetic actuation for *MSP*, *MCR*, and *MTS*, wherein **V** represents the translational velocity, **B** denotes the strength of the magnetic field, ***f*** represents the input frequency of the magnetic field, ω indicates the rotation velocity of the microsphere, and θ denotes the tilt angle between the rotation axis of the microsphere and *z* axis. (**B**) Time-lapse image sequences of the controlled locomotion of *MSP-72h*, *MCR-24h* (θ = 90°), and *MTS-24h*, with time instants marked and motion trajectories delineated. The input magnetic field strength and frequency were 7.5 mT and 10 Hz for *MSP-72h* and 7.5 mT and 5 Hz for *MCR-24h*. For *MTS-24h*, the magnetic field used is shown in fig. S9. (**C**) Velocity-frequency profiles for three-pitch *MSP-6h/24h/72h* samples in water. (**D**) Swimming performances of three-pitch *MSP-24h* in diluted blood, gastric juice, and urine (all extracted from SD rats), respectively. (C) and (D) were obtained under a magnetic field strength of 7 mT in a range of rotation frequencies. The three-pitch body length for the *MSP* samples was obtained via sonication of the *S. platensis* before the dip-coating process. The error bars represent the standard deviation of three tests.

approach to obtain large quantities of helices with similar lengths at one time.

Benefiting from the superior magnetic properties of Fe_3O_4 NPs, the *MSP*s were superparamagnetic and exhibited excellent capabilities for controlled locomotion in various fluids, including DI water (Fig. 2C and movie S1), diluted blood (Fig. 2D and movie S5), gastric juice (Fig. 2D and movie S6), urine (Fig. 2D and movie S7), and even highly viscous peanut oil (PO) (movie S8). In brief, being superparamagnetic means no remnant magnetization. This is crucial for the in vivo biomedical application of microswimmers, where usually a swarm of them is needed. It guarantees that the microswimmers are agglomeration-free and will not cause hazardous embolization during navigation through the systematic blood vasculature and/or interstitial spaces. Because what we aim to stress in this article are the functionalities of *MSP*s, the characterization of their magnetic properties and other relevant information about in vitro swimming experiments (e.g., magnetic field, microswimmer size, and fluid viscosity) are discussed in the Supplementary Materials (figs. S7, S9, and S10, and tables S2 and S3).

Fluorescence properties and sensing

Figure 3A demonstrates the fluorescence emission spectra measured in DI water for three magnetized *S. platensis* samples subject to different dip-coating time, namely, *MSP-6h*, *MSP-24h*, and *MSP-72h*. The patterns of these spectra resembled that of the untreated *S. platensis* (i.e., *MSP-0h*) in a qualitative manner, indicating that the autofluorescence of these magnetized samples had been inherited from the original microalgae. Nevertheless, the fluorescence intensity values of the emission peaks were found to be negatively correlated to the dip-coating time. This was presumably attributed to the reduced mass of *S. platensis* in unit weight as the relative proportion of Fe_3O_4 increases. Furthermore, with thicker Fe_3O_4 coating (a result of longer dip-coating time), a red shift in the emission peaks occurred (i.e., value of the corresponding wavelength increases), accompanied by widening of the full width at half maximum (FWHM). As shown in table S4, from *MSP-0h* to *MSP-72h*, the wavelength of the emission peak shifted from 651.0 to 659.4 mm, and FWHM increased from 52.1 to 57.7 nm. These variations suggested that the autofluorescence of BMRs might be tailored via controlling the dip-coating time during the fabrication process.

The stability of the fluorescent signals was examined by monitoring the emission intensity at 660 nm against the illumination time. As Fig. 3B shows, the intensity of the fluorescent signal emitted by *MSP-72h* steadily increased from 0 to 30 min (Phase I) but then leveled off (Phase II). The enhancement of fluorescence in Phase I could be explained by the increase of sample concentration due to sedimentation in the testing area (fig. S11A). As the sedimentation ended at Phase II, the fluorescent signal became stable, suggesting good photostability of the sample's autofluorescence. The fluorescence of individual microswimmers was further examined with CLSM at 552-nm excitation (fig. S11B). After 60 min illumination (light intensity, 20 W/m^2), the fluorescent signal was still stable without noticeable bleaching. We ascribe this photostability to the intact autofluorescent compounds in the biological structure (*52*, *53*).

In Fig. 3 (C to F), we characterized the fluorescence of *MPS-72h* with varying concentrations in solutions of different solvents and pH values. In Fig. 3C, the 100 μg/ml *MPS-72h* sample was found to exhibit strong fluorescent signals in neutral (pH 6.86) or alkaline (pH 9.18) solutions

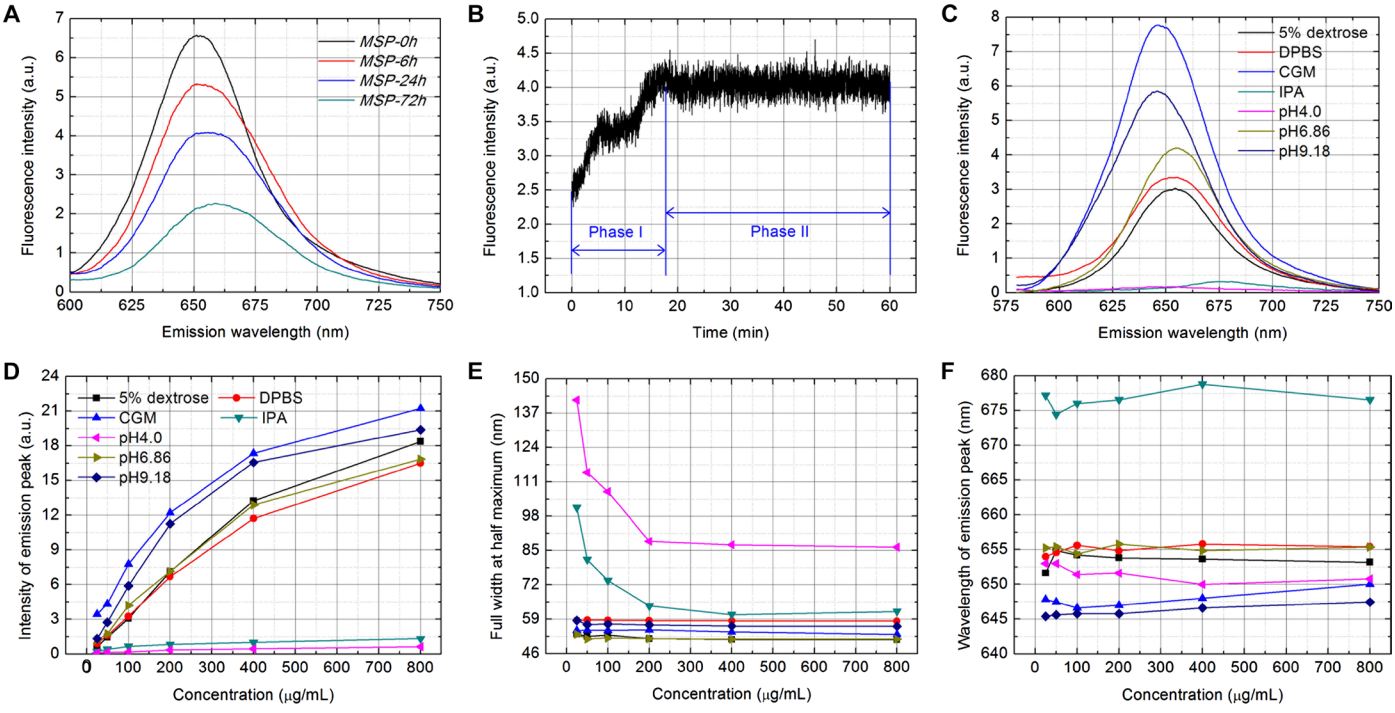

Fig. 3. Fluorescence properties of *MSP*. (**A**) Fluorescence emission spectra of *MSP-0h*, *MSP-6h*, *MSP-24h*, and *MSP-72h* (all 100 μg/ml) in DI water. (**B**) Fluorescence intensity of *MSP-72h* (100 μg/ml) versus illumination time at 660-nm emission. (**C**) Fluorescence emission spectra of *MSP-72h* (100 μg/ml) in solutions of different solvents and pH values. (**D**) Fluorescence intensity, (**E**) FWMH, and (**F**) wavelength of the emission peak for *MSP-72h* samples with varied concentration in solutions of different solvents and pH values. All fluorescent signals were recorded using a Hitachi F-7000 Fluorescence Spectrophotometer with an excitation wavelength of 552 nm.

and physiological media such as 5% dextrose, DPBS (Dulbecco's phosphate-buffered saline), and CGM (cell growth media) but relatively weak signals in acid solution (pH 4.0) and IPA (isopropyl alcohol). Despite the enhanced fluorescence intensity of the emission peak as the sample concentration increases (Fig. 3D), other fluorescence characteristics of *MSP-72h*, such as FWHM (Fig. 3E) and wavelength of the emission peak (Fig. 3F), were almost unaffected by the concentration, except some drastic changes for concentrations below 200 μg/ml in the acid solution and IPA. This feature makes the *MSP* sample a promising probe for remote diagnostic sensing, because it can sense the change of biofluidic environments associated with the onset of disease and emit distinct fluorescence free from the interference of its own concentration (*33*, *34*, *52*–*54*).

Fluorescence-based in vivo imaging

Fluorescence-based in vivo imaging experiments were performed in the subcutaneous tissue and the intraperitoneal cavity of nude mice. Subcutaneous tissues, also known as superficial fascia in anatomy, are loose substances located right below the dermis (*55*). Because they have narrow interstice and little physiological media, diffusion of the injected sample would happen slowly here, and hence, fluorescent signals can be more easily detected. Technically, these tissues are ideal positions for the study of in vivo fluorescence versus sample concentration and residence time. However, environments for microrobots to navigate in realistic medical applications are mostly complex geometries filled with biological fluids, where the injected sample may diffuse or degrade quickly. Given this, the intraperitoneal cavity, a space between the parietal peritoneum and visceral peritoneum (*56*), was also chosen for experiments. Below, we will demonstrate that, for both locations inside the mice, strong red light emission from the *MPS* samples could be easily observed upon green light excitation without addition of any fluorescent markers.

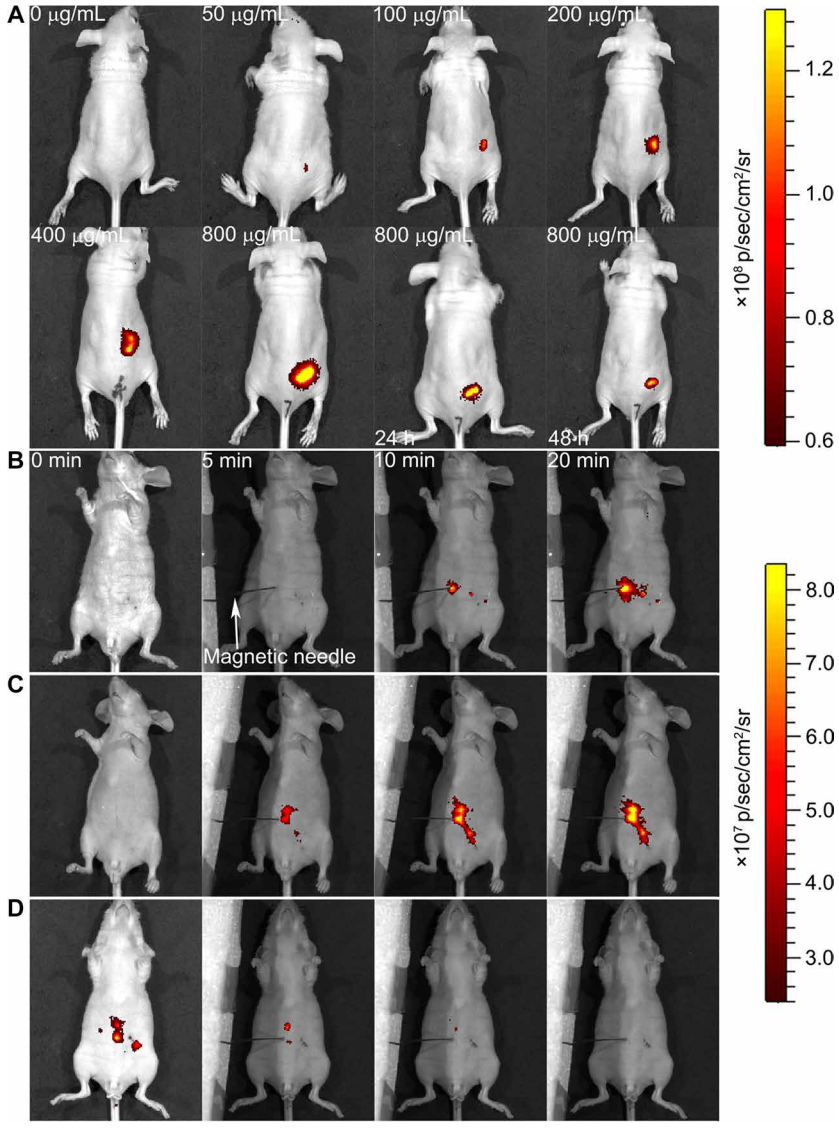

Fig. 4. Fluorescence-based in vivo imaging of *MSP*. (**A**) Fluorescence of 100 μl of *MSP-72h* with varied concentrations in the subcutaneous tissue of nude Balb/c athymic mice at three residence times. The residence time is 0 min unless otherwise specified. Fluorescence of 300 μl of (**B**) *MSP-72h*, (**C**) *MSP-24h*, and (**D**) *MSP-6h* (all 800 μg/ml) in the intraperitoneal cavity at various residence times. Image sequences of (C) and (D) were recorded at the same time intervals with (B). The magnetic needle was placed at $t = 3$ min.

As illustrated by the image sequences of *MSP-72h* with varied concentrations and residence time in the subcutaneous tissue, the fluorescence intensity increased with the sample concentration but decreased with the residence time (Fig. 4A). Quantitative analysis in fig. S12 (B and C) confirmed that the intensity of the fluorescent signal increased monotonically with the sample concentration, whereas the trend versus time was actually nonmonotonic. The fluorescent signal almost remained unchanged within the first 6 hours after injection but then went through a slight increase until reaching 15 hours, when its intensity started to drop drastically. This nonmonotonic trend was believed to have been caused by two opposing effects on the fluorescence during the biodegradation process. On the one hand, the sample's biodegradation changed the molecular environment of its autofluorescent compounds, for example, chlorophyll, which may play a dominant role at an early stage and contributed to the slight increase of fluorescence intensity (see more explanation about this effect in the "Degradation" section) (*33*, *34*, *52*–*54*). On the other hand, the absolute amount of fluorescent matter decreased as the degradation continues, which substantially affected the fluorescence and led to the drop of fluorescence intensity at a later stage. Similar trends were found for *MSP-6h* and *MPS-24h* samples, as shown in fig. S12 (B and C), and can be explained likewise.

Figure 4 (B to D) presents the imaging results of *MSP-72h*, *MSP-24h*, and *MSP-6h* in the intraperitoneal cavity. For *MSP-72h* and *MSP-24h*, no immediate fluorescent signals could be detected after injection, even with 300 μl of a high-concentration (800 μg/ml) sample. After placing a magnetic needle of about 40 mT (i.e., strength of the magnetic field measured on the tip of the needle) near the injection position from $t = 3$ min, we identified fluorescent signals 7 min later (i.e., at $t =$ 10 min). As the effect time of the magnetic field was further prolonged, the signal grew much stronger, implying more *MSP*s moving toward

the detection spot due to magnetic attraction. If the magnetic needle was removed abruptly, *MSP*s near the spot would diffuse rapidly, and the intensity of fluorescent signal dropped as a result (fig. S12A). For *MSP-6h*, the fluorescent signal could be immediately detected after injection without applying an external magnetic field. However, the injected sample dispersed quickly afterward, and subsequent addition of a magnetic field (i.e., magnetic needle) seemed useless because of the weak magnetization of *MPS-6h* (fig. S7). For a quantitative comparison of the fluorescence properties of the three samples, refer to fig. S12D. We believe that the distinct in vivo imaging results for the *MSP-72h*, *MSP-24h*, and *MSP-6h* samples may have been a compromised result of three factors: fluorescence characteristics, magnetization property, and in situ environment.

MR in vivo imaging

Fluorescence-based imaging is valuable for in vivo tracking of microrobots owing to its high and multidimensional specificity (*30*, *57*). Nevertheless, its penetration capability through tissues is limited to several centimeters, which fails to meet the requirements of many clinical applications (*58*). MR imaging, a powerful alternative imaging technique, has been widely applied in hospitals and clinics. It features excellent tissue-penetration capability, high spatial resolution, and superior tissue contrast. As mentioned in the "Fabrication" section, superparamagnetic Fe_3O_4 NPs as a common MR imaging contrast agent (*4*–*6*, *59*, *60*) have been engineered into the coating of *MSP* samples, which should endow them with capability for MR imaging. To verify this property of *MSP*, we used T_2-weighted MR imaging to investigate the in vitro MR contrast of *MSP-0h*/*6h*/*24h*/*72h* in porcine skin gelatin (type A). The MR imaging contrasts were found to be evident, depending on both the sample concentration and the Fe_3O_4 coating thickness (positively correlated to the dip-coating time). As fig. S13A shows, the imaging contrast could be notably enhanced with increased sample concentration and/or Fe_3O_4 coating thickness, and vice versa. These changes were reflected by the T_2 signal intensity, essentially related to the dipolar interaction of *MSP*s' magnetic moments with protons in water (*59*, *60*). Susceptibility artifacts happened at high concentrations (e.g., 400 and 800 μg/ml in this case), which may be harnessed as an indicator to detect high–*MSP* concentration regions for in vivo MR imaging.

On the basis of the in vitro tests, we chose *MSP-72h* for animal experiments to examine its feasibility for in vivo MR imaging, in both superficial tissues and a deep organ. For better imaging performance, the samples were dispersed in PO (first pressed) rather than in water; PO has higher T_2 signal intensity than water (fig. S13B) and can therefore prevent the solvent's imaging contrast from interfering with that of *MSP*'s. Two groups of rats were experimented. First, subcutaneous injection was conducted to deliver 100 μl each of 4 and 8 mg/ml *MSP72h*-PO solutions to the subcutaneous tissues of two Sprague-Dawley (SD) rats. Note that given the complex imaging conditions inside animals, the concentrations of *MSP* solution used for in vivo MR imaging were higher (10 times) than the two maximum concentrations for in vitro tests, namely, 400 and 800 μg/ml. Apparently, concentration-dependent contrasts nearby the injection spot (circled by blue dotted lines) could be identified through cross-sectional MR imaging, indicating locations of the injected *MSP-72h* (Fig. 5A). Second, intragastric administration was used to deliver 1 ml each of 4 and 8 mg/ml *MSP72h*-PO solutions into the stomachs of two other SD rats. The amplified dosage (by 10 times) for the second group compared with the first was to compensate for the diluting effect of gastric juice inside the rat's stomach. In such a deep organ, *MSP*'s autofluorescent signals cannot be detected, and fluorescence imaging ceases to work. For MR imaging, the results are detailed in Fig. 5B, where concentration-correlated MR contrasts (4 mg/ml < 8 mg/ml) were again identified. In both cases, the image contrast had clear borders (marked by blue dotted lines in Fig. 5B) and lay some distance away from the rat's dermis (~0.5 to 1.0 cm). Through a comparison with the MR imaging for pure PO (fig. S13B), the location of the *MSP* swarm inside the stomach can be determined. Evidently, the image contrast in the 8 mg/ml case was both greater in magnitude and more uniform in distribution within the stomach.

After the *MSP* swarm could be observed in the rat's stomach via MR imaging, an attempt was made to let them swim there in a controlled manner. To this end, two other SD rats were treated with an intragastric administration of 1 ml of 8 mg/ml *MSP72h*-PO solution. The rotating magnetic field for swarm control inside the rat stomach was provided by a rotating permanent magnet (RPM) mounted on a dc motor (see the inset in fig. S10) rather than the tri-axial Helmholtz coil system as has been previously used for in vitro swimming experiments. Compared with the latter, both the power transmission and operational flexibility are better for this experiment with the RPM manipulator, despite its nonuniform magnetic field strength and gradient-induced magnetic forces. As reported in (*61*), both axial control and radial control are available for an RPM manipulator, depending on actuation requirements. We used the axial control.

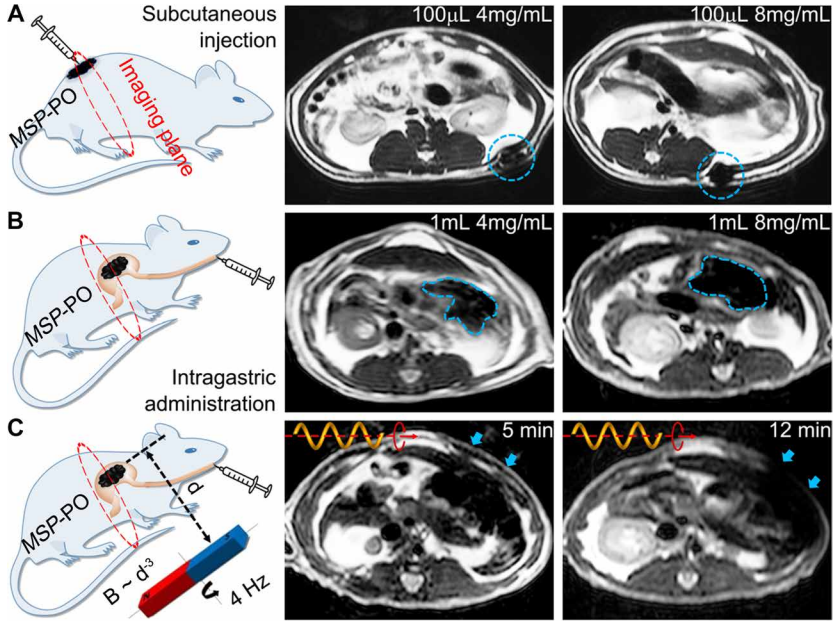

Fig. 5. T_2-weighted cross-sectional MR imaging of *MSP* swarms inside SD rats. (**A**) *MSP* swarm of two different concentrations inside the subcutaneous tissues. (**B**) *MSP* swarm of two different concentrations inside the stomachs. (**C**) *MSP* swarm with the same concentration but subject to actuation and steering (with a rotating magnetic field) of different time periods before MR imaging across the rat's stomach.

The strength of the magnetic field (**B**) acting on the rat's stomach was controlled by adjusting the vertical distance *d* between the stomach and the RPM, and its rotation frequency was controlled by adjusting the dc motor's speed of rotation. In the experiments, the positions of the rat and RPM were fixed (about 1 cm away) such that *d* varies between 2.5 and 1.5 cm (representing the outer and inner walls of the stomach, respectively), with the stomach's vertical span estimated to be 1.0 cm and its position 0.5 cm away from the skin. Within this distance, **B** was roughly 8.0 to 20.1 mT according to the measured **B**-*d* profile in fig. S10. The rotation speed of the motor was set at 240 revolutions per minute (rpm), resulting in a ration frequency of 4 Hz for the magnetic field.

By applying a proper rotating direction to the magnetic field, the *MSP-72h* swarm was easily actuated and steered toward a designated direction in vitro (see movie S8). For in vivo swimming experiments inside the rat's stomach, this direction was chosen to be the subcutaneous tissue close to the stomach. After magnetic actuation of 5 and 12 min, respectively, cross-sectional MR imaging was used to examine the location and intensity of the image contrasts within the two rats' stomachs. We observed emergence of susceptibility artifacts close to the subcutaneous tissue for both rats (indicated by blue arrows), implying the existence of high-concentration regions (rich in *MSP-72h*) nearby (Fig. 5C). Compared with the 5-min case, the susceptibility artifact at $t = 12$ min was more severe, with the stomach's MR contrast largely enclosing adjacent areas and becoming indistinguishable from the rat's dermis. To prove that the *MSP* swarm was truly actuated and steered in a controlled fashion instead of being pulled/pushed by magnetic forces from the MR equipment/permanent magnet or even simply by gastric peristalsis, we also conducted a control experiment. We repeated the MR imaging protocol for a third rat subject to a 12-min treatment using the same permanent magnet but under static state, that is, with no motor-generated rotation. No susceptibility artifact was found this time (fig. S13C), which therefore excluded the possibility of significant swarm motion due to either magnetic forces or gastric peristalsis. To conclude, the *MSP* swarm has been successfully propelled inside the rat's stomach using a rotating magnetic field and noninvasively tracked through cross-sectional MR imaging.

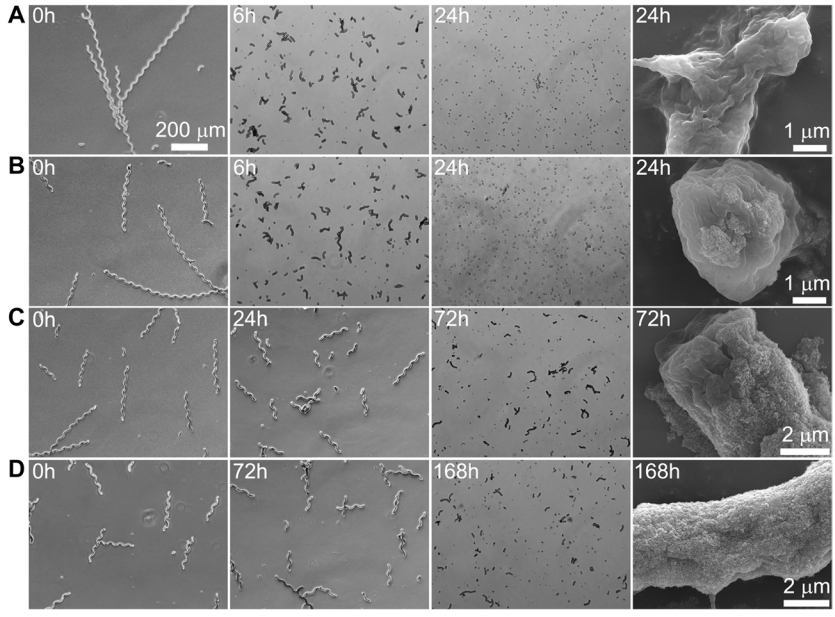

Fig. 6. Degradation of *MSP* samples in 37°C DPBS solution. (**A**) *MSP-0h*. (**B**) *MSP-6h*. (**C**) *MSP-24h*. (**D**) *MSP-72h*. In (A), the first three images are optical sequences showing the degradation process of *MSP-0h*, and the last image is a FESEM image with an enlarged view of one *MSP-0h* residue in the third optical image. (B) to (D) are organized likewise.

Degradation

All organic materials would eventually be decomposed. For BMRs (essentially composite materials), such a process should be predominantly determined by the intrinsic property of the biological matrix (organic core) that has been used to fabricate them, but we observed that the duration was subject to the influence of the engineering Fe_3O_4 coating as well. In this respect, the time span of BMR degradation can be tailored via controlling the dip-coating time. This feature would be desirable for in vivo applications, because we may have different requirements for the resident time of the injected microagents toward designated tasks, to allow navigation through vessels or cavities before they reach the targeted region and start functioning there.

The degradation of *MSP-0h/6h/24h/72h* samples was monitored and evaluated in 37°C DPBS solution. As Fig. 6A shows, *MSP-0h* degraded quickly. After 24 hours of incubation, only residual granules could be found. Similar degradation was observed for *MSP-6h* after 24 hours of incubation, except that extra Fe_3O_4 NP aggregates were found attached on the residual granules (Fig. 6B). In contrast, the degradation of *MSP-24h/72h* was much slower. After 24 hours of incubation for *MSP-24h* and 72 hours of incubation for *MSP-72h* in the DPBS solution, the helical morphology of the samples was still notable. Extended incubation to 72 hours for *MSP-24h* and 168 hours for *MSP-72h* resulted in Fe_3O_4-coated fragments (Fig. 6, C and D). Apparently, compared with *MSP-0h/6h*, the degradation process was significantly inhibited for *MSP-24h/72h* as the Fe_3O_4 coating becomes thicker, which reduced the effective contact between the organic body and the DPBS solution.

In fig. S14A, variations of the *MSP-0h/6h/24h/72h* fluorescence intensity against residence time were plotted to quantitatively monitor the course of degradation. Again, nonmonotonic trends were found. At an early stage of the degradation, the intensity of the fluorescent signal underwent a sharp increase, instead of gradually decreasing as expected (given that the absolute mass of fluorescent matter was actually reduced during degradation). This change was reminiscent of the previous in vivo imaging results for the subcutaneous tissue, where an initial increase in fluorescence intensity also happened, although much less markedly. That increase had been attributed to the degradation-induced molecular environment change of autofluorescent compounds. To verify such a conjecture, we further examined the fluorescence emission spectra of *MSP-0h*, *MSP-24h*, and *MSP-72h* at 6, 72, and 168 hours, respectively, against the controls at 0 hours (fig. S14, B to D, and table S5) in 37°C DPBS. It was revealed that blue shift of the emission peak and contraction of FWHM occurred during degradation. This alteration of fluorescence pattern ascertained the degradation-induced change of the sample's molecular environment, whose enhancing effect on the fluorescence intensity was more noteworthy for the in vitro fluorescence tests than the previous in vivo imaging inside mice.

Cytotoxicity

A nonradioactive colorimetric method, namely, 3-(4,5-dimethylthiazol-2-yl)-2,5-diphenyltetrazolium bromide (MTT) assay, was used to test the cytotoxicity of *MSP*s (see Materials and Methods for details). Three groups of MTT assays were independently carried out with a normal cell line (3T3 fibroblast cells) and two cancer cell lines (SiHa cervical cancer cells and Hep G2 liver hepatocellular carcinoma cells). All assays tested the cell viability against sample concentration and incubation time. For the 3T3 cell line, the cytotoxicity of *MSP* was very low, with 48-hour viabilities above 80% for all *MSP* samples even at high concentrations (Fig. 7A). For the cancer cell lines, the cytotoxicity turned out to be significant, especially for the SiHa cell line, whose 48-hour viability can be less than 10% if a high-concentration *MSP-0h* sample is used (Fig. 7B). For the Hep G2 cell line, the cytotoxicity of *MSP* was less potent, but still, more than 50% viability reduction can be attained with 48 hours of incubation using high-concentration *MSP-0h* (Fig. 7C). To account for the possible origin of this cytotoxicity to cancer cell lines, we have to understand the material composition of *MSP* BMRs—that is, essentially a Fe_3O_4 phase and an organic phase. In this sense, either the Fe_3O_4 NPs in the coating or the organic *Spirulina* in the core had potentially contributed to the cytotoxicity of *MSP* toward SiHa and Hep G2. According to the literature, the former is unlikely, because Fe_3O_4 NPs have been widely reported to be of low cytotoxicity (*5*, *22*, *31*, *46*). Notwithstanding, to exclude the possible interference of *MSP*'s Fe_3O_4 coating on results of the MTT assays, we tested the cytotoxicity of pure Fe_3O_4 NPs with SiHa and 3T3 cell lines. As the MTT assays in fig. S15 (A and B) revealed, to both SiHa and 3T3, the cytotoxicity of Fe_3O_4 was virtually marginal, with 48-hour cell viabilities above 80% even at Fe_3O_4 concentrations as high as 400 and 800 μg/ml. Combining these Fe_3O_4 MTT assays with the above MTT results for *MSP-0h* (Fig. 7, B and C), we infer that the significant cytotoxicity observed is most probably caused by the *Spirulina* matter remaining in *MSP*.

For more insights into this selective cytotoxicity, we used CLSM to observe fluorescein phalloidin– and 6-diamidino-2-phenylindole–stained

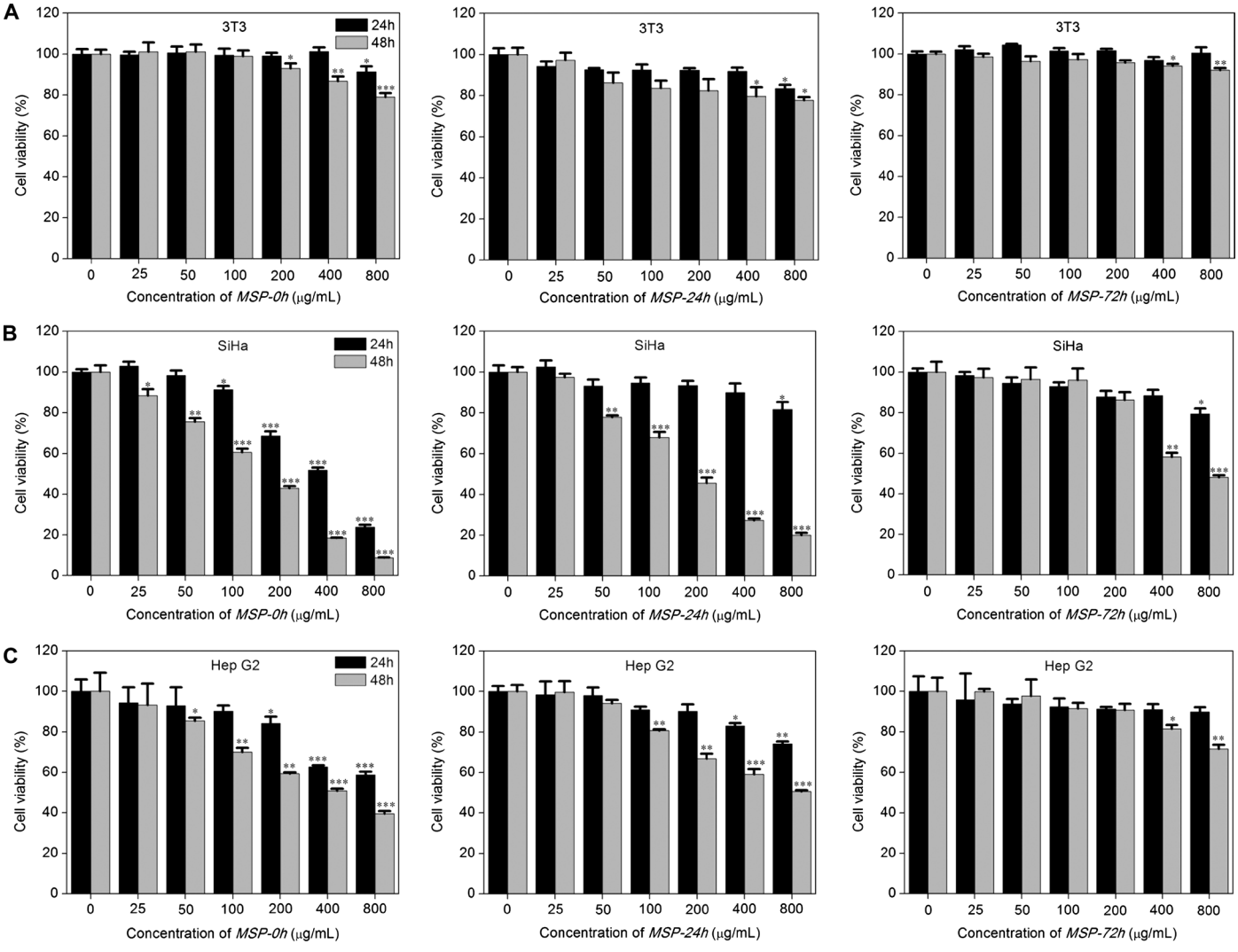

Fig. 7. Cytotoxicity of *MSP* samples to normal and cancer cell lines. (**A**) Normal cell line 3T3. (**B**) Cancer cell line SiHa. (**C**) Cancer cell line Hep G2. From left to right in each column are MTT assays for *MSP-0h*, *MSP-24h*, and *MSP-72h*. In all results, the zero-concentration group with 100% cell viability is set as the control. Six other concentration groups, that is, 25, 50, 100, 200, 400, and 800 μg/ml, are examined and compared with the control group. **P* < 0.05 is considered as statistically significant. ***P* < 0.01, ****P* < 0.001. The error bars represent the standard deviation of six independent experiments.

3T3 and SiHa cells subject to either 24 or 48 hours of incubation with two concentrations of MSP-*24h* samples, namely, 100 and 400 μg/ml. The results are displayed in fig. S16, with nuclei stained in blue and cytoskeleton stained in green. As the incubation time was prolonged, *MSP-24h* degraded into smaller segments (in red) and hence fully contacted with the cells. A major difference between the 3T3 and the SiHa cell lines as time elapsed was that the cytoskeleton network of the former remained steady, whereas that of the latter collapsed, accompanied by large-scale detachment of cells and drastic reduction of cell viability, especially at the higher concentration (400 μg/ml) of *MSP-24h*. From the morphological evolution of the SiHa cells and the scattered distribution of *MSP-24h* fragments, no sign of cell internalization or endocytosis (of *MSP* fragments) could be identified, and all *MSP* fragments appeared to be adhering to the surfaces of individual cells. Hence, the substance from *MSP* that arrested the cycle of cancer cells was seemingly released outside the cell, that is, into the culture medium. On the basis of the aforementioned results, we believe that the apoptosis of SiHa cells was most probably attributed to a specific interaction between the membrane of cancer cells and certain active biocompounds released to the culture medium due to *MSP-24h* degradation.

Biocompounds contained in *Spirulina* include phycocyanin, biopeptides, biopolymers, oligoelements, essential fatty acids, γ-linolenic acids, sterols, minerals, chlorophyll, carbohydrate, and so forth. Combined together, they endow *Spirulina* with conducive bioactivities such as antioxidant, antifungus, anti-allergy, anti-inflammation, and immunomodulation (*40*, *44*, *62*, *63*). Among others, phycocyanin, a phycobiliprotein constituting about 20% of *Spirulina* dry weight, was extensively studied in recent years for its various pharmacological properties (*64*–*69*). There has been increasing evidence that phycocyanin, or particularly C-phycocyanin (also known as C-PC), can arrest the cell cycle of cancer cells and further induce apoptosis to them, including leukemia (*67*), HeLa (*70*), squamous cell carcinoma/colorectal adenocarcinoma (*68*), and Hep G2 (*69*). The specificity of C-PC's toxicity toward tumor cells rather than toward normal cells has also been discussed (*68*, *71*). In view of those works, the selective cytotoxicity of *MSP* samples to cancer cells we observed during MTT assays was parallel to findings about C-PC in the literature. There may be more complex processes associated with biocompounds from *Spirulina* other than C-PC, but exhaustive experiments are needed to elaborate this, preferably in collaboration with biologists. In sum, we hypothesize that the active biocompounds released from the *Spirulina* matter during degradation, such as phycocyanin, have caused selective cytotoxicity, that is, inhibiting cancer cell lines (SiHa and Hep G2) rather than 3T3 normal cells.

Next, we took the MTT assay results with the SiHa cell line as an example, where the cytotoxicity was most potent, to explore how this cytotoxicity varied between different *MSP* samples and under different assay conditions. We show (Fig. 7B) the cell viability of SiHa cancer cell line subject to two sets of incubation time (i.e., 24 and 48 hours) with *MSP-0h*/*24h*/*72h* of varying concentrations (the cytotoxicity behavior of *MSP-6h* was similar to that of *MSP-0h*; therefore, we skip its results here for brevity). For all *MSP* samples, a longer dip-coating time during fabrication meant a thicker Fe_3O_4 coating on the surface (i.e., *MSP-0h* < *MSP-24h* < *MSP-72h*), which had two implications. First, the proportion of organic matter, and hence anticancer biocompounds, in unit weight of *MSP* sample was smaller. Second, the degradation, and therefore degradation-induced release of biocompounds, was slower. These two aspects combined together accounted for the much stronger cytotoxicity of *MSP-0h* and *MSP-24h* compared with *MSP-72h*. For a given *MSP* sample, the cytotoxicity it manifests was co-determined by the absolute amount of biocompounds and the release of these biocompounds. Consequently, its cytotoxicity could be enhanced either by increasing the sample concentration (i.e., from 25 to 800 μg/ml) or by prolonging the incubation time (i.e., from 24 to 48 hours). In light of the latter approach, pre-degradation of the sample before MTT assay, which contributes to the release of biocompounds, should also increase the cytotoxicity. This conjecture was verified by SiHa MTT assays with *MSP-24h* and *MSP-72h* samples subject to 24 hours of pre-degradation in cell growth media (fig. S15, C and D). There was an increase in cytotoxicity compared with the original samples without pre-degradation (Fig. 7B).

DISCUSSION

We report a type of biohybrid magnetite microrobot that is imageable, biodegradable, and selectively cytotoxic to cancer cells. The fabrication uses a facile one step–only approach using magnetite NPs, which is cost-effective and suitable for large-scale production. Our results suggest that the fabricated biohybrid microagent is capable of performing robust navigation in various biofluids and being noninvasively tracked by autofluorescence/MR imaging in either superficial tissues or deep organs. Furthermore, it exhibits desired biodegradability, remote diagnostic sensing ability, and anticancer potential. With its features of in vivo monitor via bimodal imaging, tunable degradation via dip-coating control, and inclusiveness of functionality extension/drug loading via surface modification, this biohybrid microagent represents a microbiorobotic vehicle with a high potential for imaging-guided therapy. Furthermore, it may have far-reaching significance as a proof of concept for the development of microrobots and nanorobots with multiple functions.

As suggested by Li *et al.* (*2*), the application of microrobots and nanorobots for health care issues is still at its infancy stage, especially regarding targeted therapy. Until now, controlled navigation and cargo-towing using microrobots and nanorobots have mostly been performed in vitro, and only a few in vivo studies have emerged recently (*30*, *57*, *72*–*76*). In the context of magnetic microrobots and nanorobots, a technological breakthrough was made by Servant *et al.* (*30*), who controlled and monitored in real time a swarm of artificial bacterial flagella (ABFs) in the peritoneal cavity of a mouse via magnetic actuation and fluorescence imaging. Notwithstanding the accomplishment, critical challenges such as surface interaction, device degradation, and in vivo toxicity persisted; the microswimmers might not be suitable for clinic trials on account of their chemical composition (Ni/Ti-coated and NIR-797–stained polymeric helices). Subsequent work by Peters *et al.* (*22*) addressed these issues by adopting a cross-linked hydrogel composite material to fabricate the ABFs. However, the capabilities of fluorescence imaging and motion tracking for those hydrogel ABFs as a swarm in vivo have yet to be examined. Meanwhile, because the fabrication was still confined to clean room processing, the feasibility of cost-effective batch production of such microswimmers for medical purposes needs to be further assessed.

With biohybrid superparamagnetic microrobots reported in this work, we set out to resolve the challenges faced by Servant *et al.* (*30*) from another perspective: to directly engineer smart materials in nature, that is, microalgae. By integrating the biological materials with low-cytotoxicity magnetite NPs while preserving the desirable functional

attributes of both elements, the fabricated microrobots can attain multifunctional capabilities with a one step–only approach. In particular, we have highlighted several important functionalities of the microrobots aimed at imaging-guided therapy, such as bimodal in vivo imaging capability (consisting of autofluorescence-based imaging for superficial tissues/cavities and inherent MR contrast for both superficial and deep tissues/organs), tunable biodegradation (adjusted by duration of the dip-coating process), and selective cytotoxicity to cancer cells (owing to the pharmacological biocompounds released from *Spirulina* during degradation). Furthermore, we have accomplished in vivo monitored locomotion inside rats' stomachs, where a large swarm of such microrobots (up to circa 1 million) are propelled by an external rotating magnetic field and tracked by cross-sectional MR imaging in a deep organ. Nevertheless, to ultimately realize imaging-guided therapy using these microrobots, several essential aspects remain to be explored in our future work: (i) the loading/release capability of extra diagnostic/therapeutic cargo, (ii) in vivo residence subject to the adverse effect of potential host responses, (iii) the navigation of a swarm to lesion location, and (iv) the in vivo diagnostic/therapeutic effect on lesions, for example, malignant tumors. One specific aspect worth immediate attention is the intriguing *Spirulina*-induced apoptosis to cancer cells, whose specificity is of profound importance for nanomedicine and may open the door to a series of innovative therapies for cancer treatment. To reveal the full mechanism behind this phenomenon and therefore enable medical applications, a great endeavor remains to be made in collaboration with biologists and oncologists.

MATERIALS AND METHODS

Materials

Saccharomyces cerevisiae, pine pollen (disruption powder), and kapok fiber were purchased from the market; lotus vessel was extracted from the roots of lotus; and human hair was cut from author X.Y. *Rhodospirillum rubrum* was provided by P. Wu (Harbin University of Commerce); *S. platensis*, *C. reinhardtii*, *T. subcordiformis*, and *Chlorella salina* were provided by Y. Zhang (Qingdao Agricultural University); and the cell growth medium was provided by L. Bian (Chinese University of Hong Kong). Ferric chloride ($FeCl_3$), ferrous chloride tetrahydrate ($FeCl_2{\cdot}4H_2O$), and dextrose monohydrate were purchased from Acros Organics (Thermo Fisher Scientific Inc., USA); sodium hydroxide (NaOH, ≥98%, pellets) was purchased from Aladdin (China); hydrochloric acid (HCl, 5 M) was purchased from BDH Prolabo (VWR International S.A.S., France), absolute ethanol and IPA were purchased from EMSURE (EMD Millipore Corporation, Germany); porcine skin gelatin (type A) was purchased from Sigma-Aldrich (USA); and DPBS was purchased from Gibco (Thermo Fisher Scientific Inc., USA). Buffer solutions of pH 4.0, pH 6.86, and pH 9.18 were prepared using calibration buffer powder of a CHEETAH pH meter (PHS-3C). The fibroblast cell line 3T3, the cancer cell line SiHa, and the liver hepatocellular carcinoma cell line Hep G2 were obtained from ATCC (USA). All chemical regents were used without further purification.

Synthesis of Fe_3O_4 NP suspensions

Fe_3O_4 NP suspensions were prepared based on the co-precipitation method (*41*, *45*, *46*), with a typical process conducted in a KUSON ultrasonic bath (degas modal, 20 kHz, 0.35 W/cm^2). First, 10 ml of NaOH solution (0.5 M) was added dropwise to an aqueous $FeCl_3$ (0.008 M)–$FeCl_2$ (0.016 M) mixture at 50°C, resulting in a black suspension. Second, after sonication for 60 min, the black suspension was repeatedly centrifuged (10,000 rpm, 15 min) and redispersed in DI water (via sonication) three times. Last, 100 μl of HCl solution (5 M) was added to the final redispersed suspension, followed by further sonication for 60 min. Then, positive-charged Fe_3O_4 NP suspensions (circa pH 2.1) were obtained.

Dip-coating process

The dip-coating process of biological matrices was carried out at ambient temperature and pressure in a solution (circa pH 3.0) of the above Fe_3O_4 NP suspension dispersed in 50 ml of DI water, containing about 9.28 mg of magnetite NPs (dry weight). All biological samples were washed three times with DI water before they were added to the solution. To shorten their body length, we additionally sonicated the *S. platensis* sample for 15 min (20 kHz, 0.35 W/cm^2). The dip-coating process was performed without any continuous hard shaking. Only intermittent soft shaking was applied to avoid the agglomeration of biological samples. After the dip-coating process, the final products were separated by centrifugation and then stocked in DI water.

Structural characterization

Optical images were captured by an OLYMPUS optical microscope connected to a PC with a charge-coupled device camera. FESEM images were acquired using a FEI Quanta 400F microscope with an accelerating voltage of 10 kV. To enhance their conductivity, all samples went through gold sputtering at 10 mA for 45 s using an SC 502 Ion Sputter Coating Machine (POLARON) unless otherwise specified. Transmission electron microscopy images were acquired using a FEI Tecnai Spirit electron microscope with an accelerating voltage of 200 kV. Element analysis was carried out with an EDX analyzer (mounted on the FEI Quanta 400F) with an accelerating voltage of 20 kV. An x-ray diffraction test was conducted on a Smartlab (Rigaku) diffractometer using Cu target (40 kV, 40 mA). Transmission Fourier transform infrared (FTIR) test was conducted in a Thermo Scientific Nicolet iS10 FTIR spectrometer using the typical KBr pressed disc technique (2 mg of sample and 200 mg of KBr). All FESEM samples, either magnetized or not, were freeze-dried in an ilShinBioBase freeze dryer (TFD8503) unless otherwise specified.

Characterization of magnetic, propulsion, and fluorescence properties

Magnetic properties of the magnetic microrobots were measured using a vibrating sample magnetometer (VSM; PPMS Model 6000 Quantum Design) at room temperature. The propulsion tests were conducted using either homogeneous rotating or periodically varying magnetic fields generated by a custom-built tri-axial Helmholtz coil system. The bright-field and fluorescence images were taken in DI water using a Leica SP8 confocal laser scanning microscope. The fluorescence spectra were recorded using a Hitachi F-7000 Fluorescence Spectrophotometer equipped with an L2175 Xenon lamp (HAMAMATSU). The testing resolution was 1.0 nm, and the testing parameters were set as follows: scanning rate at 1200 nm/min; excitation and emission slit width at 5.0 nm. High-pass emission filters of 420, 500, and 580 nm were used for the 405-, 488-, and 552-nm excitation, respectively.

Fluorescence-based in vivo imaging

In vivo imaging experiments based on *MPS*'s autofluorescence were performed in the subcutaneous tissue and intraperitoneal cavity of

Balb/c athymic mice, which were bred and kept at the Laboratory Animal Services Center of the Chinese University of Hong Kong. The 6-, 24-, and 72-hour dipping *S. platensis* were dispersed in 1 ml of DI water to obtain solutions with concentrations of 0, 50, 100, 200, 400, and 800 μg/ml. The as-prepared solutions were then irradiated by ultraviolet light for 1 hour for sterilization before injection. Experiments of in vivo imaging were conducted as follows: (i) The mice were anesthetized by ketamine (75 mg/kg)/xylazine (10 mg/kg) and laid flat on a rigid support, and (ii) all mice were implemented with subcutaneous injection (100 μl) or intraperitoneal injection (300 μl). The subcutaneous group was immediately imaged with a DsRed excitation filter and a 660-nm emission filter using an IVIS 200 imaging system (Xenogen Imaging Technologies, Alameda, CA), and the intraperitoneal group was imaged every 5 min. For experiments of fluorescence intensity against residence time, 12 mice were subcutaneously injected in a biological safety cabinet (1300 Series A2, Thermo Fisher Scientific Inc., USA) and then returned to the Laboratory Animal Services Center of the Chinese University of Hong Kong to continue breeding. The fluorescent signals were recorded at 15, 24, 48, and/or 72 hours, respectively.

T_2-weighted in vitro MR imaging

All MR images were captured in a water bath (20 cm × 12 cm × 8 cm) placed within a transmit-receive head coil using a 3.0-T clinical whole-body MR unit (Achieva TX; Philips Medical Systems, Best, Netherlands). T_2-weighted MR imaging was measured using a standard Carr-Purcell-Meiboom-Gill pulse sequence, with TR (time of repetition) = 2000 ms, TE (time of echo) range = 30 to 960 ms, 32 echoes, field of view = 134 × 67 mm, matrix = 128 × 64, slice thickness = 5 mm. To ensure that the distribution of *MSP* is homogeneous during MR imaging, all tested samples were fixed with porcine skin gelatin (type A) in 1.5-ml centrifuge tubes (Thermo Fisher Scientific Inc., USA).

T_2-weighted in vivo MR imaging

Female SD rats (250 to 280 g), bred and kept at the Laboratory Animal Services Center of the Chinese University of Hong Kong, were used for animal experiments. The experimental protocols were approved by the Animal Experimentation Ethics Committee of the Chinese University of Hong Kong and licensed by the Department of Health of Hong Kong SAR. For MR imaging in the subcutaneous tissue, two SD rats were anaesthetized with ketamine (80 mg/kg)/xylazine (10 mg/kg) via intraperitoneal injection and laid flat on a rigid support. They were subjected to subcutaneous injection with 100 μl each of 4 and 8 mg/ml *MSP72h*-PO solutions and then sequentially placed inside a 3.0-T clinical MR scanner for MR imaging (Achieva TX; Philips Medical Systems, Best, Netherlands). The radiofrequency transmitter and receiver was a human wrist coil. For MR imaging of stomach, another three rats were fed via intragastric administration of 1 ml of PO, 1 ml of 4 mg/ml *MSP72h*-PO solution, and 1 ml of 8 mg/ml *MSP72h*-PO solution. After 5 min, each rat was anaesthetized with ketamine (80 mg/kg)/xylazine (10 mg/kg) via intraperitoneal injection and fixed in the same scanner for MR imaging. Three more rats were fed with 8 mg of *MSP-72h* per 1 ml of PO, anaesthetized with ketamine, and then treated with different magnetic fields. The first two were treated for 5 and 12 min, respectively, with an RPM, and the third rat was treated for 12 min with the same permanent magnet but without rotation. The following are the main MR imaging parameters: turbo spin echo sequence, TR = 4200 ms, TE = 80 ms, flip angle = 90°, slice thickness = 3 mm, number of excitations = 4, echo train length = 16, pixel size = 0.2 mm × 0.2 mm.

Degradation experiments

Tests of biodegradability were conducted for 0-/6-/24-/72-hour dipping *S. platensis*. Each sample (freeze-dried, 2 mg) was added into a Thermo Scientific Nunc 50-ml conical centrifuge tube containing 20 ml of DPBS and then incubated in a 5% CO_2–95% air humidified atmosphere at 37°C. At each designed time point, 500-, 100-, and 50-μl samples were successively removed from the tube and respectively characterized using fluorescence spectrophotometry, FESEM, and optical microscopy. The extracted FESEM samples were washed three times with DI water via centrifugation.

Cell culture and subculture

The fibroblast cell line 3T3 was cultured with minimum essential media at 37°C in a 5% CO_2–95% air humidified atmosphere. When the cell confluence reached circa 75 to 80%, the cells were washed by sterile PBS. Next, the trypsin was neutralized (Invitrogen, CA, USA) by full medium and washed with PBS. Then, the cells were collected via centrifugation (1000*g* for 5 min). Subsequently, the cell pellet was resuspended with fresh full medium and passaged to four plastic tissue culture dishes (100 mm). Last, they were incubated at 37°C in a 5% CO_2–95% air humidified atmosphere for proliferation. The cervical cancer cell line SiHa was cultured with the same protocol.

MTT assay

MTT assay was performed for *MSP* samples with three cell lines, including the fibroblast cell line 3T3, the cervical cancer cell line SiHa, and the liver hepatocellular carcinoma cell line Hep G2. All experiments were repeated three times for verification. 3T3, SiHa, and Hep G2 cells were separately seeded into three 96-well (4000 cells per well) culture plates (Invitrogen) and cultured at 37°C in a 5% CO_2–95% air humidified atmosphere. After 24 hours of incubation for cells to adhere, the culture medium was replaced with a fresh medium containing *MSP* samples with concentrations of 0, 25, 50, 100, 200, 400, and 800 μg/ml (six replicate wells for each concentration, with a final volume of 100 μl per well). After another 24 or 48 hours of incubation, the culture medium was carefully removed, and the cells were washed twice with PBS. Subsequently, 150 μl of MTT (0.5 mg/ml) was added. After 4 hours of incubation, the culture medium was again carefully removed, and 150 μl of DMSO per well was added, followed by 10 min of shaking on a horizontal shaker. Absorbance was read using enzyme-labeling analysis equipment (Biotek Synergy 2, BioTek, USA) at 570 nm. The average absorbance yields the result of cell viability.

Immunofluorescence staining

3T3 and SiHa cells were seeded on glasses placed in six-well plates (10,000 cells per well). Each well was filled with 2.5 ml of Dulbecco's modified Eagle's medium, including 10% fetal bovine serum and 1% penicillin-streptomycin. After 24 hours of incubation, *MSP-24h* (0, 100, and 400 μg/ml) samples were added and cocultured with the 3T3 and SiHa cells for 24 and 48 hours. At designated time instants (i.e., 24 and 48 hours), cell-covered glasses were taken out from the plate wells, followed by three repeated rinses with PBS (Gibco). The rinsed cells on glasses were subsequently treated with 30 min of fixation in 4% paraformaldehyde (Sigma-Aldrich). After washing three times with PBS, the fixed cells were soon dipped into 0.3% Triton X-100 (Sigma-Aldrich) for 30 min. Next, permeabilized cells were blocked for 30 min with 2% bovine serum albumin (Sigma-Aldrich). Then, these pretreated cells were ready to be stained. Cytoskeleton

staining was performed with 90-min incubation of the pretreated cells in PBS-diluted fluorescein phalloidin (200:1, volume ratio), and nuclei counterstaining was carried out with 30-min incubation in PBS-diluted 6-diamidino-2-phenylindole (1:1000, volume ratio) after washing three times with 0.1 weight % Tween 20 (PBS). To avoid photobleaching, all staining processes were performed in a dark environment. All steps for the immunofluorescence staining were performed at room temperature. The fluorescence images were then captured using a Zeiss LSM 700 confocal laser scanning microscope.

SUPPLEMENTARY MATERIALS

robotics.sciencemag.org/cgi/content/full/2/12/eaaq1155/DC1
Section S1. Autofluorescence of biological materials
Section S2. Dip-coating *S. platensis* with Fe_3O_4 NPs
Section S3. Magnetic actuation of BMRs
Section S4. Fluorescence properties and in vivo imaging
Section S5. MR imaging in vitro and in vivo
Section S6. Degradation of *MSP*s
Section S7. Cytotoxicity to SiHa and 3T3 cell lines
Fig. S1. Autofluorescence of biological materials with various structures.
Fig. S2. Characterizing the autofluorescence of *S. platensis*, pine pollen, and *S. cerevisiae*.
Fig. S3. Photostability tests in DI water for *S. platensis* (100 μg/ml), *S. cerevisiae* (1 mg/ml), and *C. salina* (100 μg/ml).
Fig. S4. Characterization of *S. platensis* (i.e., *MSP-0h*) and Fe_3O_4 NPs.
Fig. S5. ζ potential of *S. platensis* and Fe_3O_4 NP suspension at different pH.
Fig. S6. Characterization of the magnetized *S. platensis*.
Fig. S7. Magnetic hysteresis loops of *MSP-6h/24h/72h* (300 K, via VSM).
Fig. S8. FESEM images of *MSP-72h* that has undergone a 5-min sonication treatment.
Fig. S9. The periodically varying magnetic field for the actuation of *MTS-24h*.
Fig. S10. Strength of the magnetic field generated by the permanent magnet B versus the distance *d* to its rotation axis.
Fig. S11. Photostability test of *MSP-72h*.
Fig. S12. Supplementary data for fluorescence-based in vivo imaging.
Fig. S13. T_2-weighted MR imaging of *MSP* samples in vitro and in vivo.
Fig. S14. Degradation of *MSP* in 37°C DPBS solution.
Fig. S15. Supplementary data for cytotoxicity evaluation.
Fig. S16. CLSM imaging for 3T3 and SiHa cells cocultured with *MSP-24h* samples (0, 100, and 400 μg/ml) for 24 and 48 hours.
Table S1. Quantitative measurement of Fe contents in *MSP-6h/24h/72h* samples.
Table S2. Main distribution of body length (in pitches) for *MSP* samples under different conditions.
Table S3. Viscosity of various fluids for in vitro/in vivo swimming experiments.
Table S4. Quantitative data of the emission peaks for *MSP-0h/6h/24h/72h* samples in Fig. 3A.
Table S5. Quantitative data of the emission peaks for *MSP-0h/24h/72h* samples before and after degradation.
Movie S1. Magnetic actuation of three-pitch *MSP-72h* in DI water using a rotating magnetic field (7.5 mT and 10 Hz).
Movie S2. Magnetic actuation of *MCR-24h* (θ = 90°) in DI water using a rotating magnetic field (7.5 mT and 5 Hz).
Movie S3. Magnetic actuation of *MCR-24h* (θ = 0°) in DI water using a rotating magnetic field (7.5 mT and 3 Hz).
Movie S4. Magnetic actuation of *MTS-24h* in water using a periodically varying magnetic field described in fig. S9.
Movie S5. Magnetic actuation of three-pitch *MSP-24h* in diluted blood using a rotating magnetic field (7 mT and 6 Hz).
Movie S6. Magnetic actuation of three-pitch *MSP-24h* in gastric juice using a rotating magnetic field (7 mT and 8 Hz).
Movie S7. Magnetic actuation of three-pitch *MSP-24h* in urine using a rotating magnetic field (7 mT and 4 Hz).
Movie S8. In vitro magnetic actuation of a *MSP-72h* swarm in PO (first pressed).
References (*77*–*79*)

REFERENCES AND NOTES

1. B. J. Nelson, I. K. Kaliakatsos, J. J. Abbott, Microrobots for minimally invasive medicine. *Annu. Rev. Biomed. Eng.* **12**, 55–85 (2010).
2. J. Li, B. E.-F. de Ávila, W. Gao, L. Zhang, J. Wang, Micro/nanorobots for biomedicine: Delivery, surgery, sensing, and detoxification. *Sci. Robot.* **2**, eaam6431 (2017).
3. M. Sitti, H. Ceylan, W. Hu, J. Giltinan, M. Turan, S. Yim, E. Diller, Biomedical applications of untethered mobile milli/microrobots. *Proc. IEEE* **103**, 205–224 (2015).
4. S. Martel, Beyond imaging: Macro- and microscale medical robots actuated by clinical MRI scanners. *Sci. Robot.* **2**, eaam8119 (2017).
5. P. Vartholomeos, M. Fruchard, A. Ferreira, C. Mavroidis, MRI-guided nanorobotic systems for therapeutic and diagnostic applications. *Annu. Rev. Biomed. Eng.* **13**, 157–184 (2011).
6. S. Martel, M. Mohammadi, O. Felfoul, Z. Lu, P. Pouponneau, Flagellated magnetotactic bacteria as controlled MRI-trackable propulsion and steering systems for medical nanorobots operating in the human microvasculature. *Int. J. Robot. Res.* **28**, 571–582 (2009).
7. S. Tottori, L. Zhang, F. Qiu, K. K. Krawczyk, A. Franco-Obregón, B. J. Nelson, Magnetic helical micromachines: Fabrication, controlled swimming, and cargo transport. *Adv. Mater.* **24**, 811–816 (2012).
8. W. Wang, L. A. Castro, M. Hoyos, T. E. Mallouk, Autonomous motion of metallic microrods propelled by ultrasound. *ACS Nano* **6**, 6122–6132 (2012).
9. S. Palagi, A. G. Mark, S. Y. Reigh, K. Melde, T. Qiu, H. Zeng, C. Parmeggiani, D. Martella, A. Sanchez-Castillo, N. Kapernaum, F. Giesselmann, D. S. Wiersma, E. Lauga, P. Fischer, Structured light enables biomimetic swimming and versatile locomotion of photoresponsive soft microrobots. *Nat. Mater.* **15**, 647–653 (2016).
10. V. Magdanz, S. Sanchez, O. G. Schmidt, Development of a sperm-flagella driven micro-bio-robot. *Adv. Mater.* **25**, 6581–6588 (2013).
11. R. W. Carlsen, M. Sitti, Bio-hybrid cell-based actuators for microsystems. *Small* **10**, 3831–3851 (2014).
12. W. F. Paxton, K. C. Kistler, C. C. Olmeda, A. Sen, S. K. St. Angelo, Y. Cao, T. E. Mallouk, P. E. Lammert, V. H. Crespi, Catalytic nanomotors: Autonomous movement of striped nanorods. *J. Am. Chem. Soc.* **126**, 13424–13431 (2004).
13. W. Gao, K. M. Manesh, J. Hua, S. Sattayasamitsathit, J. Wang, Hybrid nanomotor: A catalytically/magnetically powered adaptive nanowire swimmer. *Small* **7**, 2047–2051 (2011).
14. J. Li, T. Li, T. Xu, M. Kiristi, W. Liu, Z. Wu, J. Wang, Magneto-acoustic hybrid nanomotor. *Nano Lett.* **15**, 4814–4821 (2015).
15. R. S. M. Rikken, R. J. M. Nolte, J. C. Maan, J. C. M. van Hest, D. A. Wilson, P. C. M. Christianen, Manipulation of micro- and nanostructure motion with magnetic fields. *Soft Matter* **10**, 1295–1308 (2014).
16. L. Zhang, T. Petit, Y. Lu, B. E. Kratochvil, K. E. Peyer, R. Pei, J. Lou, B. J. Nelson, Controlled propulsion and cargo transport of rotating nickel nanowires near a patterned solid surface. *ACS Nano* **4**, 6228–6234 (2010).
17. B. Jang, E. Gutman, N. Stucki, B. F. Seitz, P. D. Wendel-García, T. Newton, J. Pokki, O. Ergeneman, S. Pané, Y. Or, B. J. Nelson, Undulatory locomotion of magnetic multilink nanoswimmers. *Nano Lett.* **15**, 4829–4833 (2015).
18. S. Fusco, M. S. Akar, S. Kennedy, C. Peters, R. Bottani, F. Starsich, A. Mao, G. A. Sotiriou, S. Pané, S. E. Pratsinis, D. Mooney, B. J. Nelson, An integrated microrobotic platform for on-demand, targeted therapeutic interventions. *Adv. Mater.* **26**, 952–957 (2014).
19. Z. Ye, M. Sitti, Dynamic trapping and two-dimensional transport of swimming microorganisms using a rotating magnetic microrobot. *Lab Chip* **14**, 2177–2182 (2014).
20. C. Pawashe, S. Floyd, M. Sitti, Modeling and experimental characterization of an untethered magnetic micro-robot. *Int. J. Robot. Res.* **28**, 1077–1094 (2009).
21. S. Tasoglu, E. Diller, S. Guven, M. Sitti, U. Demirci, Untethered micro-robotic coding of three-dimensional material composition. *Nat. Commun.* **5**, 3124 (2014).
22. C. Peters, M. Hoop, S. Pané, B. J. Nelson, C. Hierold, Degradable magnetic composites for minimally invasive interventions: Device fabrication, targeted drug delivery, and cytotoxicity tests. *Adv. Mater.* **28**, 533–538 (2016).
23. D. Walker, B. T. Käsdorf, H.-H. Jeong, O. Lieleg, P. Fischer, Enzymatically active biomimetic micropropellers for the penetration of mucin gels. *Sci. Adv.* **1**, e1500501 (2015).
24. P. L. Venugopalan, R. Sai, Y. Chandorkar, B. Basu, S. Shivashankar, A. Ghosh, Conformal cytocompatible ferrite coatings facilitate the realization of a nanovoyager in human blood. *Nano Lett.* **14**, 1968–1975 (2014).
25. D. Schamel, A. G. Mark, J. G. Gibbs, C. Miksch, K. I. Morozov, A. M. Leshansky, P. Fischer, Nanopropellers and their actuation in complex viscoelastic media. *ACS Nano* **8**, 8794–8801 (2014).
26. R. Dreyfus, J. Baudry, M. L. Roper, M. Fermigier, H. A. Stone, J. Bibette, Microscopic artificial swimmers. *Nature* **437**, 862–865 (2005).
27. P. J. Vach, P. Fratzl, S. Klumpp, D. Faivre, Fast magnetic micropropellers with random shapes. *Nano Lett.* **15**, 7064–7070 (2015).
28. H.-W. Huang, M. S. Sakar, A. J. Petruska, S. Pané, B. J. Nelson, Soft micromachines with programmable motility and morphology. *Nat. Commun.* **7**, 12263 (2016).
29. M. Medina-Sánchez, L. Schwarz, A. K. Meyer, F. Hebenstreit, O. G. Schmidt, Cellular cargo delivery: Toward assisted fertilization by sperm-carrying micromotors. *Nano Lett.* **16**, 555–561 (2015).

30. A. Servant, F. Qiu, M. Mazza, K. Kostarelos, B. J. Nelson, Controlled in vivo swimming of a swarm of bacteria-like microrobotic flagella. *Adv. Mater.* **27**, 2981–2988 (2015).
31. X. Yan, Q. Zhou, J. Yu, T. Xu, Y. Deng, T. Tang, Q. Feng, L. Bian, Y. Zhang, A. Ferreia, L. Zhang, Magnetite nanostructured porous hollow helical microswimmers for targeted delivery. *Adv. Funct. Mater.* **25**, 5333–5342 (2015).
32. A. M. Maier, C. Weig, P. Oswald, E. Frey, P. Fischer, T. Liedl, Magnetic propulsion of microswimmers with DNA-based flagellar bundles. *Nano Lett.* **16**, 906–910 (2016).
33. J. Christensen, L. Norgaard, R. Bro, S. B. Engelsen, Multivariate autofluorescence of intact food systems. *Chem. Rev.* **106**, 1979–1994 (2006).
34. N. Billinton, A. W. Knight, Seeing the wood through the trees: A review of techniques for distinguishing green fluorescent protein from endogenous autofluorescence. *Anal. Biochem.* **291**, 175–197 (2001).
35. P. Fratzl, R. Weinkamer, Nature's hierarchical materials. *Prog. Mater. Sci.* **52**, 1263–1334 (2007).
36. P.-Y. Chen, J. McKittrick, M. A. Meyers, Biological materials: Functional adaptations and bioinspired designs. *Prog. Mater. Sci.* **57**, 1492–1704 (2012).
37. A. R. Parker, H. E. Townley, Biomimetics of photonic nanostructures. *Nat. Nanotechnol.* **2**, 347–353 (2007).
38. R. Blakemore, Magnetotactic bacteria. *Science* **190**, 377–379 (1975).
39. R. Pethig, Dielectric properties of biological materials: Biophysical and medical applications. *IEEE Trans. Elect. Insul.* **EI-19**, 453–474 (1984).
40. B. Metting, J. W. Pyne, Biologically active compounds from microalgae. *Enzyme Microb. Technol.* **8**, 386–394 (1986).
41. T.-X. Fan, S.-K. Chow, D. Zhang, Biomorphic mineralization: From biology to materials. *Prog. Mater. Sci.* **54**, 542–659 (2009).
42. C. Sanchez, H. Arribart, M. M. G. Guille, Biomimetism and bioinspiration as tools for the design of innovative materials and systems. *Nat. Mater.* **4**, 277–288 (2005).
43. H. Wang, M. Pumera, Fabrication of micro/nanoscale motors. *Chem. Rev.* **115**, 8704–8735 (2015).
44. P. Spolaore, C. Joannis-Cassan, E. Duran, A. Isambert, Commercial applications of microalgae. *J. Biosci. Bioeng.* **101**, 87–96 (2006).
45. E. L. Mayes, F. Vollrath, S. Mann, Fabrication of magnetic spider silk and other silk-fiber composites using inorganic nanoparticles. *Adv. Mater.* **10**, 801–805 (1998).
46. A.-H. Lu, E. L. Salabas, F. Schüth, Magnetic nanoparticles: Synthesis, protection, functionalization, and application. *Angew. Chem. Int. Ed. Engl.* **46**, 1222–1244 (2007).
47. J. J. Abbott, K. E. Peyer, M. C. Lagomarsino, L. Zhang, L. Dong, I. K. Kaliakatsos, B. J. Nelson, How should microrobots swim? *Int. J. Robot. Res.* **28**, 1434–1447 (2009).
48. P. Fischer, A. Ghosh, Magnetically actuated propulsion at low Reynolds numbers: Towards nanoscale control. *Nanoscale* **3**, 557–563 (2011).
49. K. E. Peyer, L. Zhang, B. J. Nelson, Bio-inspired magnetic swimming microrobots for biomedical applications. *Nanoscale* **5**, 1259–1272 (2013).
50. J. Rahmer, C. Stehning, B. Gleich, Spatially selective remote magnetic actuation of identical helical micromachines. *Sci. Robot.* **2**, eaal2845 (2017).
51. W. Gao, X. Feng, A. Pei, C. R. Kane, R. Tam, C. Hennessy, J. Wang, Bioinspired helical microswimmers based on vascular plants. *Nano Lett.* **14**, 305–310 (2014).
52. R. N. Dsouza, U. Pischel, W. M. Nau, Fluorescent dyes and their supramolecular host/guest complexes with macrocycles in aqueous solution. *Chem. Rev.* **111**, 7941–7980 (2011).
53. S. Silvi, A. Credi, Luminescent sensors based on quantum dot–molecule conjugates. *Chem. Soc. Rev.* **44**, 4275–4289 (2015).
54. S. Ohkuma, B. Poole, Fluorescence probe measurement of the intralysosomal pH in living cells and the perturbation of pH by various agents. *Proc. Natl. Acad. Sci. U.S.A.* **75**, 3327–3331 (1978).
55. P. T. C. So, H. Kim, I. E. Kochevar, Two-photon deep tissue ex vivo imaging of mouse dermal and subcutaneous structures. *Opt. Express* **3**, 339–350 (1998).
56. P. W. Tank, J. C. B. Grant, *Grant's Dissector* (Lippincott Williams & Wilkins, 2012).
57. J. Li, S. Thamphiwatana, W. Liu, B. Esteban-Fernández de Ávila, P. Angsantikul, E. Sandraz, J. Wang, T. Xu, F. Soto, V. Ramez, Enteric micromotor can selectively position and spontaneously propel in the gastrointestinal tract. *ACS Nano* **10**, 9536–9542 (2016).
58. V. Ntziachristos, J. Ripoll, L. V. Wang, R. Weissleder, Looking and listening to light: The evolution of whole-body photonic imaging. *Nat. Biotechnol.* **23**, 313–320 (2005).
59. Y.-X. J. Wang, S. Xuan, M. Port, J.-M. Idee, Recent advances in superparamagnetic iron oxide nanoparticles for cellular imaging and targeted therapy research. *Curr. Pharm. Des.* **19**, 6575–6593 (2013).
60. Y.-X. J. Wang, J.-M. Idee, A comprehensive literatures update of clinical researches of superparamagnetic resonance iron oxide nanoparticles for magnetic resonance imaging. *Quant. Imaging Med. Surg.* **7**, 88–122 (2017).
61. T. W. Fountain, P. V. Kailat, J. J. Abbott, in *2010 IEEE International Conference on Robotics and Automation (ICRA)* (IEEE, 2010), pp. 576–581.
62. A. Belay, Y. Ota, K. Miyakawa, H. Shimamatsu, Current knowledge on potential health benefits of *Spirulina*. *J. Appl. Phycol.* **5**, 235–241 (1993).
63. O. Ciferri, *Spirulina*, the edible microorganism. *Microbiol. Rev.* **47**, 551–578 (1983).
64. V. B. Bhat, K. Madyastha, C-phycocyanin: A potent peroxyl radical scavenger in vivo and in vitro. *Biochem. Biophys. Res. Commun.* **275**, 20–25 (2000).
65. B. V. V. Pardhasaradhi, A. M. Ali, A. L. Kumari, P. Reddanna, A. Khar, Phycocyanin-mediated apoptosis in AK-5 tumor cells involves down-regulation of Bcl-2 and generation of ROS. *Mol. Cancer Ther.* **2**, 1165–1170 (2003).
66. Ch. Romay, R. Gonzalez, N. Ledon, D. Remirez, V. Rimbau, C-phycocyanin: A biliprotein with antioxidant, anti-inflammatory and neuroprotective effects. *Curr. Protein Pept. Sci.* **4**, 207–216 (2003).
67. J. Subhashini, S. V. K. Mahipal, M. C. Reddy, M. M. Reddy, A. Rachamallu, P. Reddanna, Molecular mechanisms in C-phycocyanin induced apoptosis in human chronic myeloid leukemia cell line-K562. *Biochem. Pharmacol.* **68**, 453–462 (2004).
68. H. Wang, Y. Liu, X. Gao, C. L. Carter, Z.-R. Liu, The recombinant β subunit of C-phycocyanin inhibits cell proliferation and induces apoptosis. *Cancer Lett.* **247**, 150–158 (2007).
69. O. M. Basha, R. A. Hafez, Y. M. El-Ayouty, K. F. Mahrous, M. H. Bareedy, A. M. Salama, C-Phycocyanin inhibits cell proliferation and may induce apoptosis in human HepG2 cells. *Egypt. J. Immunol.* **15**, 161–167 (2008).
70. B. Li, M.-H. Gao, X.-C. Zhang, X.-M. Chu, Molecular immune mechanism of C-phycocyanin from *Spirulina platensis* induces apoptosis in HeLa cells in vitro. *Biotechnol. Appl. Biochem.* **43**, 155–164 (2006).
71. E. F. e Silva, F. da Silva Figueira, A. P. Lettnin, M. Carrett-Dias, D. de Moraes Vaz Batista Filgueira, S. Kalil, G. S. Trindade, A. P. de Souza Votto, C-Phycocyanin: Cellular targets, mechanisms of action and multi drug resistance in cancer. *Pharmacol. Rep.* (2017); https://doi.org/10.1016/j.pharep.2017.07.018 (paper published online before print).
72. W. Gao, R. Dong, S. Thamphiwatana, J. Li, W. Gao, L. Zhang, J. Wang, Artificial micromotors in the mouse's stomach: A step toward in vivo use of synthetic motors. *ACS Nano* **9**, 117–123 (2015).
73. O. Felfoul, M. Mohammadi, S. Taherkhani, D. De Lanauze, Y. Z. Xu, D. Loghin, S. Essa, S. Jancik, D. Houle, M. Lafleur, L. Gaboury, M. Tabrizian, N. Kaou, M. Atkin, T. Vuong, G. Batist, N. Beauchemin, D. Radzioch, S. Martel, Magneto-aerotactic bacteria deliver drug-containing nanoliposomes to tumour hypoxic regions. *Nat. Nanotechnol.* **11**, 941–947 (2016).
74. B. Esteban-Fernández de Ávila, P. Angsantikul, J. Li, M. A. Lopez-Ramirez, D. E. Ramírez-Herrera, S. Thamphiwatana, C. Chen, J. Delezuk, R. Samakapiruk, V. Ramez, L. Zhang, J. Wang, Micromotor-enabled active drug delivery for in vivo treatment of stomach infection. *Nat. Commun.* **8**, 272 (2017).
75. F. Ullrich, C. Bergeles, J. Pokki, O. Ergeneman, S. Erni, G. Chatzipirpiridis, S. Pané, C. Framme, B. J. Nelson, Mobility experiments with microrobots for minimally invasive intraocular surgery. *Invest. Ophthalmol. Vis. Sci.* **54**, 2853–2863 (2013).
76. G. Chatzipirpiridis, O. Ergeneman, J. Pokki, F. Ullrich, S. Fusco, J. A. Ortega, K. M. Sivaraman, B. J. Nelson, S. Pané, Electroforming of implantable tubular magnetic microrobots for wireless ophthalmologic applications. *Adv. Healthcare Mater.* **4**, 209–214 (2015).
77. F. C. Meldrum, H. Cölfen, Controlling mineral morphologies and structures in biological and synthetic systems. *Chem. Rev.* **108**, 4332–4432 (2008).
78. S. Sotiropoulou, Y. Sierra-Sastre, S. S. Mark, C. A. Batt, Biotemplated nanostructured materials. *Chem. Mater.* **20**, 821–834 (2008).
79. T. Zhang, W. Wang, D. Zhang, X. Zhang, Y. Ma, Y. Zhou, L. Qi, Biotemplated synthesis of gold nanoparticle–bacteria cellulose nanofiber nanocomposites and their application in biosensing. *Adv. Funct. Mater.* **20**, 1152–1160 (2010).

Acknowledgments: We thank D. Yung and N. So (Division of Biomedical Engineering, Chinese University of Hong Kong) for offering instruments to prepare materials; J. Chen (Department of Obstetrics and Gynaecology, Chinese University of Hong Kong) for help with animal experiments; W. Y.-W. Lee (Department of Orthopaedics and Traumatology, Chinese University of Hong Kong) for helping operate the IVIS system; Y. Zhang (College of Resources and Environment, Qingdao Agricultural University) and X. Wang (College of Marine Science and Engineering, Qingdao Agricultural University) for cultivating *S. platensis*, *C. reinhardtii*, *T. subcordiformis*, and *C. salina*; and P. Wu (Harbin University of Commerce) for providing *R. rubrum*. Also, we thank V. Chan (Centre for Cell and Developmental Biology, Chinese University of Hong Kong), C. W. Lin (Department of Chemistry, Chinese University of Hong Kong), and Q. Li, A. Li, and M. H. Yeung (Department of Physics, Chinese University of Hong Kong) for help with the structural and fluorescent characterization of material as well as discussions on results. Q.Z. would like to thank the University of Edinburgh for the award of a Principal's Career Development Scholarship and an Edinburgh Global Research Scholarship. **Funding:** This research was financially supported by the Early Career Scheme grant with project no. 439113 and the General Research Fund with project nos. 14209514, 14203715, and 14218516 from the Research Grants Council of Hong Kong. **Author contributions:** X.Y. conceived the idea, designed and conducted the experiments, analyzed the results, and wrote the manuscript. Q.Z. contributed to the analysis of results and co-wrote the manuscript. M.V. and K.K. repeated the experiments on degradation and cytotoxicity and discussed the

results. Y.D. and T.T. supported all in vivo experiments involving the use of animals. J.Y. performed the swimming experiments for *MSP* and *MCR*. J.X. and L.B. supported the experiments on fluorescence characterization and material degradation. T.X. performed the swimming experiment for *MTS*. Y.-X.J.W. performed the MR imaging experiments. L.Z. supervised this work, guided the discussion, and edited the manuscript. **Competing interests:** The authors declare that they have no competing financial interests. **Data and materials availability:** All data needed to evaluate the conclusions in the paper are present in the paper and/or the Supplementary Materials. Additional data related to this paper may be requested from the corresponding author via email.

Submitted 24 April 2017
Resubmitted 4 October 2017
Accepted 3 November 2017
Published 22 November 2017
10.1126/scirobotics.aaq1155

Citation: X. Yan, Q. Zhou, M. Vincent, Y. Deng, J. Yu, J. Xu, T. Xu, T. Tang, L. Bian, Y.-X. J. Wang, K. Kostarelos, L. Zhang, Multifunctional biohybrid magnetite microrobots for imaging-guided therapy. *Sci. Robot.* **2**, eaaq1155 (2017).

Science Robotics

Multifunctional biohybrid magnetite microrobots for imaging-guided therapy

Xiaohui Yan, Qi Zhou, Melissa Vincent, Yan Deng, Jiangfan Yu, Jianbin Xu, Tiantian Xu, Tao Tang, Liming Bian, Yi-Xiang J. Wang, Kostas Kostarelos, and Li Zhang

Sci. Robot. **2** (12), eaaq1155. DOI: 10.1126/scirobotics.aaq1155

Science Robotics (ISSN 2470-9476) is published by the American Association for the Advancement of Science. 1200 New York Avenue NW, Washington, DC 20005. The title *Science Robotics* is a registered trademark of AAAS.